

See discussions, stats, and author profiles for this publication at: <https://www.researchgate.net/publication/264429313>

Cavitation on Deterministically Nanostructured Surfaces in Contact with an Aqueous Phase: A Small-Angle Neutron Scattering Study

ARTICLE in LANGMUIR · AUGUST 2014

Impact Factor: 4.46 · DOI: 10.1021/la500963q · Source: PubMed

READS

116

9 AUTHORS, INCLUDING:



Jitendra Bahadur

Bhabha Atomic Research Centre

61 PUBLICATIONS 353 CITATIONS

[SEE PROFILE](#)



Lilin He

Oak Ridge National Laboratory

38 PUBLICATIONS 463 CITATIONS

[SEE PROFILE](#)



Vitaliy Pipich

Forschungszentrum Jülich

58 PUBLICATIONS 552 CITATIONS

[SEE PROFILE](#)



Noémi Kinga Székely

Forschungszentrum Jülich

31 PUBLICATIONS 165 CITATIONS

[SEE PROFILE](#)

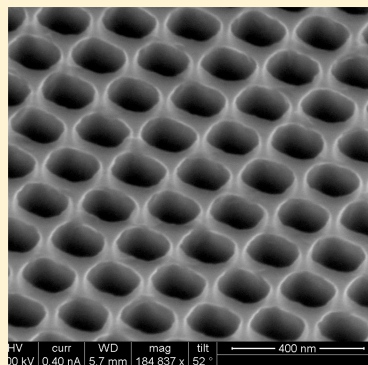
Cavitation on Deterministically Nanostructured Surfaces in Contact with an Aqueous Phase: A Small-Angle Neutron Scattering Study

Yuri B. Melnichenko,^{*,†} N. V. Lavrik,[‡] E. Popov,[§] J. Bahadur,[†] L. He,[†] I. I. Kravchenko,[‡] G. Smith,[†] V. Pipich,^{||} and N. K. Szekely^{||}

[†]Biology and Soft Matter Division, [‡]Center for Nanophase Materials Sciences, and [§]Reactor and Nuclear Systems Division, Oak Ridge National Laboratory, Oak Ridge, Tennessee 37831, United States

^{||}Forschungszentrum Jülich GmbH, JCNS at MLZ, D-85747 Garching, Germany

ABSTRACT: The structure of deterministically nanopatterned surfaces created using a combination of electron beam lithography and reactive ion etching was evaluated using small-angle neutron scattering (SANS). Samples exhibit 2D neutron scattering patterns that confirm the presence of ordered nanoscale cavities consistent with the targeted morphologies as well as with SEM data analysis. Comparison of SANS intensities obtained from samples in air and in contact with an aqueous phase (pure deuterium oxide, D₂O, or a contrast matched mixture of D₂O + H₂O) reveals formation of stable gaseous nanobubbles trapped inside the cavities. The relative volume of nanobubbles depends strongly on the hydrophobicity of the cavity walls. In the case of hydrophobic surfaces, nanobubbles occupy up to 87% of the total cavity volume. The results demonstrate the high degree of sensitivity of SANS measurements for detecting and characterizing nano- and mesoscale bubbles with the volume fraction as low as $\sim 10^{-6}$.



INTRODUCTION

Bubble formation on solid surfaces immersed in liquids plays a critical role in initiating heterogeneous pool boiling, an effective mode of heat transfer in a wide variety of natural and industrial processes.¹ Better understanding of various scenarios at the initial stage of gas phase nucleation on solid surfaces is important in predicting and controlling various boiling regimes and maximizing cooling efficiency in systems, such as nuclear reactors, where an exceedingly high amount of heat is generated in comparatively small volumes.^{2,3} Although several models have been developed to predict the nucleation site density and its impact on the heat transfer properties,^{4,5} detailed experimental information about how, where, and how many nano- and mesoscopic bubbles form on various surface morphologies under different thermodynamic conditions is still lacking. While there is a general agreement that the key processes governing gas phase nucleation occur on nano- and mesoscopic scales, the majority of experimental studies have been limited to mesoscopic and macroscopic observations^{5,6} due to numerous challenges associated with direct experimental probing of the initial stages of gas nucleation at the nanoscale.⁷ Small-angle X-ray scattering (SAXS) and small-angle neutron scattering (SANS) techniques are widely used to characterize vapor adsorption and capillary condensation in nanoporous and mesoporous solids.^{8–14} Synchrotron SAXS has also been recently applied to investigate nanowetting of superhydrophobic surfaces as well as the morphology of air bubbles trapped inside nanometer-scale hydrophobic cavities.^{15–17}

To gain further insights in this area, we used SANS as well as contrast matching SANS to study the degree of water penetration into cavities with fixed depth but different

wettability. The model nanopatterned surfaces studied in this work are lithographically patterned silicon wafers with a monolayer of highly uniform, periodic, densely packed cylindrical cavities with axes oriented perpendicular to the surface (Figure 1). The cavities are approximately 100 nm deep and 100 nm in diameter forming a 2D hexagonal grid. In order to increase the signal-to-noise ratio, we created large-area (few cm²) nanopatterned surfaces taking advantage of the deterministic nanopatterning strategy that is based on a combination of electron beam lithography and anisotropic reactive ion etching.¹⁸ The key variable parameter in the present study is surface wettability, which was tuned by modifying the patterned silicon surface with an ultrathin fluoropolymer layer.¹⁹ Consistent with recent experimental studies,^{15–17} our results confirm the hypothesis that both structural properties and chemical modification of the surfaces are critical for controlling interfacial gas nucleation²⁰ and spontaneous dewetting of the hydrophobic nanopores.²¹ Our results demonstrate that SANS is sensitive enough to characterize an interfacial 2D array of cylindrical nanopores with characteristic sizes in the 100 nm range and quantify its aqueous fill fractions. Therefore, SANS can be extremely beneficial for future studies of the bubble nucleation on metal surfaces that have been primarily characterized using macroscopic observations.^{3,5,22–26}

Received: April 8, 2014

Revised: June 19, 2014

Published: August 1, 2014

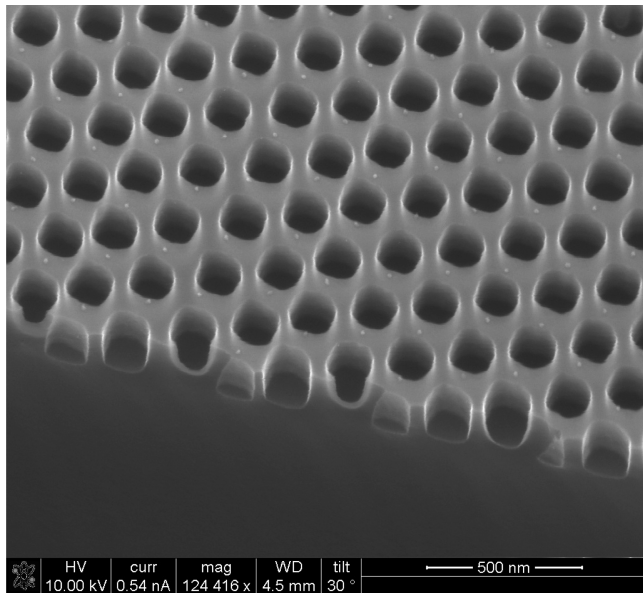


Figure 1. SEM image of the cleaved nanostructured surface.

■ EXPERIMENTAL SECTION

Sample Preparation. Nanopatterning of 100 mm diameter silicon wafers started with deposition of 3000 Å thick electron beam resist (ZEP-520A, Zeon Corp.; Tokyo, Japan) followed by exposure using a JEOL 9300-FS electron beam lithography system. Exposed patterns were developed in xylene for 30 s, rinsed with isopropanol, and dried with nitrogen gas. The remaining resist pattern was used as an etch mask for anisotropic etching of Si with an Oxford Plasmalab 100 inductively coupled plasma reactive ion etching system at an etch rate of ~1500 Å/min (Oxford Instruments, Concord, MA). Etching was timed to obtain ~1000 Å deep holes. Residual photoresist was removed from the patterned samples in *N*-methyl-2-pyrrolidone at 70 °C. Samples were subsequently rinsed with deionized water and dried with a stream of filtered nitrogen. Oxygen plasma was used as a final cleaning step.

For the current experiments two samples were prepared. Sample 1 is a nanostructured Si wafer covered with an approximately 2 nm layer of naturally occurring silicon oxide (native oxide). Sample 2 has an additional 5 nm layer of a strongly hydrophobic fluoropolymer deposited in plasma using C₄F₈ as a precursor gas as described previously.¹⁹ The native oxide and fluoropolymer thicknesses were measured ellipsometrically using a satellite silicon wafer with a smooth surface. The nanoscale morphology was evaluated using FEI Nova 500 SEM. The wettability of the prepared surfaces was analyzed using a Rame-Hart telescopic goniometer equipped with a Gil mont syringe.

Average contact angles measured for sample 1 and sample 2 after completing the SANS experiments were found to be 35° and 65°, respectively.

SANS Experiments. Custom-built liquid tight copper sample holders were used in these experiments. The schematic of the sample holders used in the experiments is shown in Figure 2. Front windows of the holders were made of 1 mm thick unpatterned Si wafers virtually transparent to neutrons. Wafers with the nanopatterned surfaces looking inside the cell served as exit windows. The front and rear windows are thermally isolated, and their temperature can be independently controlled using Peltier elements (PE) to better than ±0.1 °C using a precision temperature controller. Such design allows for measuring scattering from nanobubbles on the sample extremely close to the boiling temperature without inducing boiling in the bulk of the surrounding liquid (option not used in the current experiment). The internal cell volume may be filled with liquid with the total liquid thickness in the holder ~4 mm.

In addition, nonpatterned SiO₂ and fluoropolymer covered wafers were prepared and scattering from these wafers put in place of the corresponding nanostructured samples was subtracted as a background from scattering measured from the actual samples. Samples were aligned perpendicular to the beam (cavities parallel to the beam) to better than ±0.1°. SANS measurements with samples in air were conducted after drying them in a vacuum oven at 60 °C for 2 h. After completing these measurements, sample cells were filled with either degassed D₂O or a degassed contrast matched (D₂O + H₂O) mixture. The neutron beam size used was about 4.5 cm² in area, and acquisition times were of the order of 3 h. The total data acquisition time of 3 h was split into six half-hour runs, which were analyzed individually to check for possible changes of the bubble sizes with time. As long as the scattering data had no time dependence, the data were summed and averaged to increase the data quality.

Two-dimensional SANS patterns from both samples in air, in contact with D₂O, and immersed in CMS are shown in Figure 3. Such patterns are typical for diffraction data obtained from a two-dimensional array of hexagonally packed cylinders with the axes parallel to the beam. The position of main Bragg peak was evaluated using the focusing mirror very small-angle scattering (VSANS) diffractometer (KWS-3) (neutron wavelength $\lambda = 12.8 \text{ \AA}$, $\Delta\lambda/\lambda \sim 0.20$) available at the Heinz Maier-Leibnitz FRM-II reactor. SANS experiments were performed at the Heinz Maier-Leibnitz FRM-II reactor on a KWS-2 instrument (experiment 1) and at ORNL using the General Purpose SANS instrument (experiment 2) using $\lambda = 9.8 \text{ \AA}$ ($\Delta\lambda/\lambda \sim 0.20$) and $\lambda = 12 \text{ \AA}$ ($\Delta\lambda/\lambda \sim 0.13$), respectively. The sample-detector distance was chosen to cover an overall range of scattering vectors (Q) $0.0015 < Q < 0.015 \text{ \AA}^{-1}$, where $Q = 4\pi\lambda^{-1} \sin \theta$, in which 2θ is the scattering angle. The data were corrected for instrumental background, sample transmission, and detector efficiency. In experiment 1, SANS was measured from samples in air and samples immersed in D₂O. These measurements were repeated in experiment 2 in order to double check the reproducibility of the previous results.

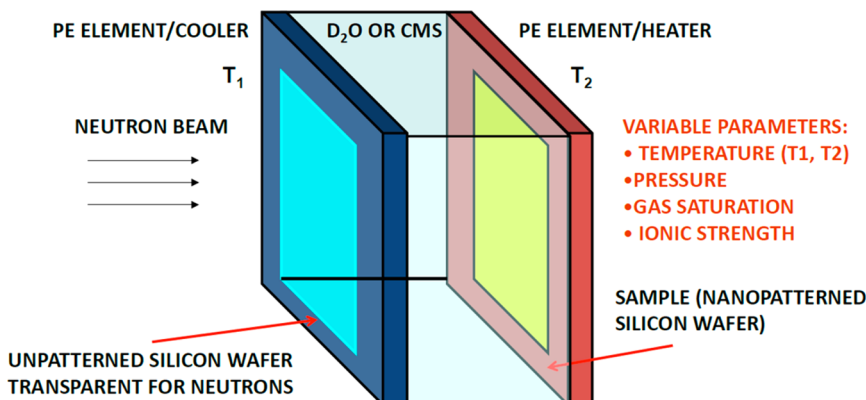


Figure 2. Schematic of the sample holders.

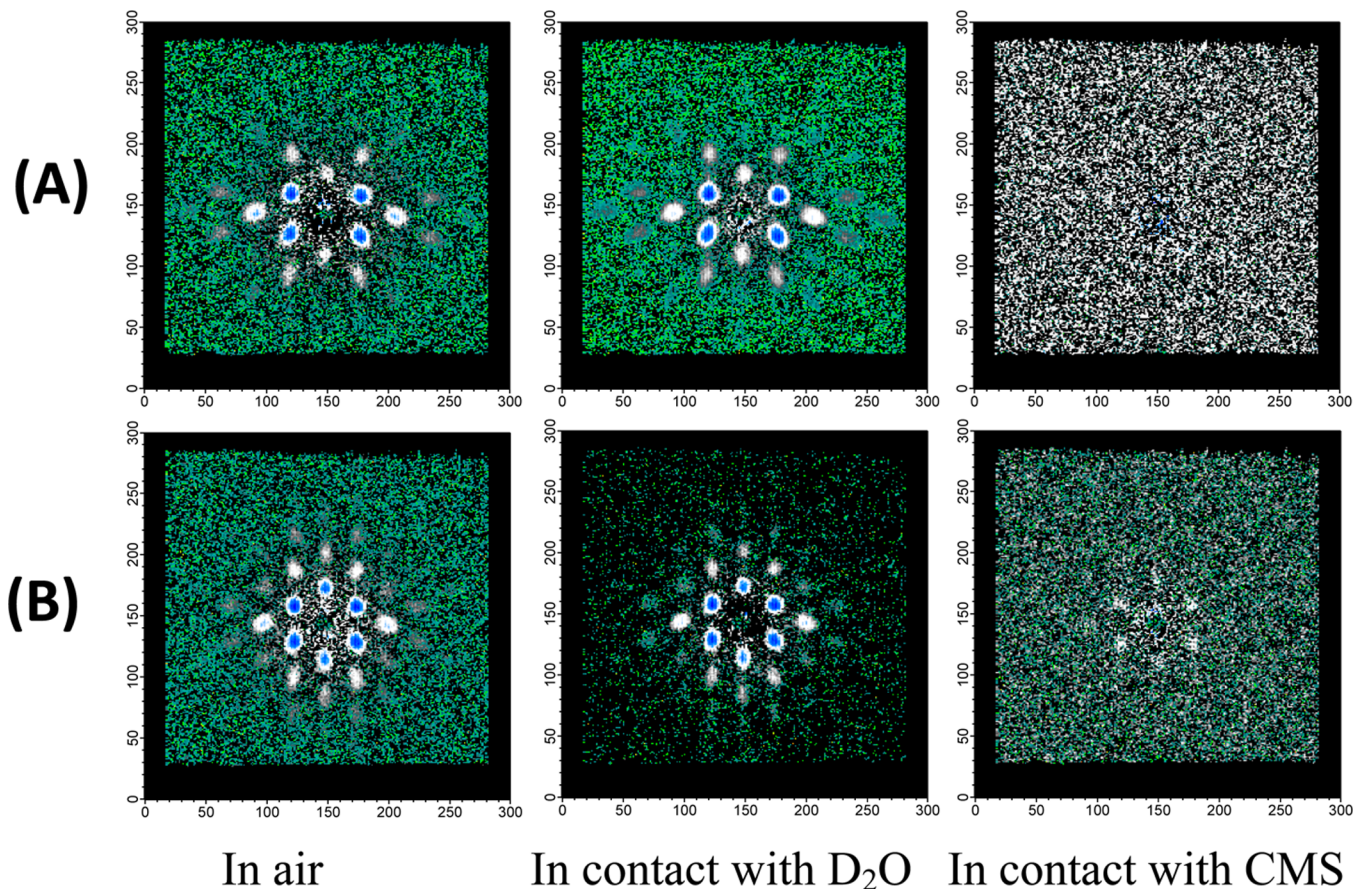


Figure 3. Two-dimensional SANS patterns from sample 1 (A) and sample 2 (B) nanostructured wafers in contact with air, D_2O , and contrast matched solution of $\text{D}_2\text{O} + \text{H}_2\text{O}$.

In addition, SANS was measured from both sample 1 and 2 in contact with contrast matched solution (CMS) of (40.85 wt % $\text{D}_2\text{O} + 59.15$ wt % H_2O) with an average scattering length density (SLD) matching that of Si wafer matrix (Table 1).

Table 1. Physical Densities and Calculated Scattering Length Densities (SLDs) of the Relevant Solids and Liquids

compound	chemical formula	physical density (g/cm^3)	SLD (10^{10} cm^{-2})
silicon	Si	2.34	2.08
silica	SiO_2	2.2	3.47
PTFE	$\text{C}_{10}\text{H}_4\text{Cl}_3\text{F}_{17}\text{Si}$	1.7	3.18
deuterium oxide	D_2O	1.06	6.39
water	H_2O	1	-0.56
contrast matching solution (CMS)	40.85% $\text{D}_2\text{O} +$ 59.15% H_2O	1.04	2.08

Diffractograms of up to 3 orders may be resolved for samples in contact with D_2O due to highly uniform patterning. Typical radially averaged scattering curves for samples 1 and 2 are shown in Figures 4 and 5, respectively. The position of the first-order peaks for samples in air and in contact with D_2O is observed at $Q_{10} = 0.0037 \text{ \AA}^{-1}$, corresponding to the 10 reflection of the two-dimensional hexagonal lattice. This permits determination of the center-to-center distance between the cavities from the position of the main peak in Q -space by using the equation¹² $d = 4\pi/(Q_{10}\sqrt{3}) = 1960 \text{ \AA}$, which is in good agreement with the distance between cavities of 2000 \AA estimated from the SEM images shown in Figure 1. The secondary peaks are weaker but still detectable at positions $Q = 0.0061$ and 0.0092 \AA^{-1} , corresponding to the 11 and 21 reflections, respectively. As is seen in Table 1, neutron contrast between Si and D_2O ($2.08 \times 10^{10} \text{ cm}^{-2} -$

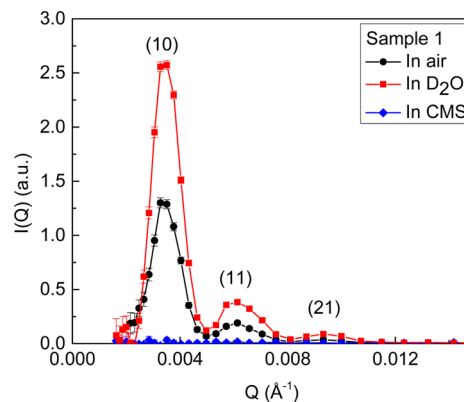


Figure 4. Bragg peaks from sample 1 in air and/or in contact with D_2O and with contrast matched solution of $\text{D}_2\text{O} + \text{H}_2\text{O}$ measured in experiment 2.

$6.39 \times 10^{10} \text{ cm}^{-2})^2 \approx 18.6 \times 10^{20} \text{ cm}^{-4}$ is much higher than that between Si and air filled cavities ($2.08 \times 10^{10} \text{ cm}^{-2})^2 \approx 4.3 \times 10^{20} \text{ cm}^{-4}$, which implies that water penetration into the cavities should lead to increase of the amplitude of the observed peaks. The intensity of all peaks actually increases after immersing samples in D_2O ; however, the degree of the increase is smaller for the more hydrophobic sample 2 (see Figures 4 and 5 and Table 2). After immersing in contrast matching solution, the scattering from sample 1 becomes unmeasurable within the experimental error. At the same time, the SANS from sample 2 in contact with the CMS shows small but measurable residual scattering (see Figures 3–5).

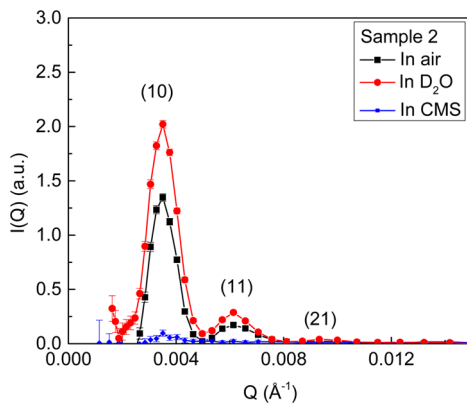


Figure 5. Bragg peaks from sample 2 in air and or in contact with D_2O and with contrast matched solution of $D_2O + H_2O$ measured in experiment 2.

Table 2. Main Bragg Peak (10) Amplitudes, Peak Amplitude Ratios Normalized to the Amplitude of the Peak from Samples in Air, and Corresponding Volume Fraction of Liquid (D_2O or CMS) in Cavities

expt	sample no.	condition	amplitude	peak ratio	cavity filling degree
1	1	in air	1.32		
1	2	in air	1.32		
1	1	in D_2O	2.85	2.16	0.39
1	2	in D_2O	1.93	1.46	0.13
2	1	in air	1.30		
2	2	in air	1.35		
2	1	in D_2O	2.57	1.98	0.34
2	2	in D_2O	2.02	1.50	0.14
2	1	in CMS	~0	~0	
2	2	in CMS	0.056	0.041	0.19

Geometric Model. The small-angle scattering intensity $I(Q)$ from an array of parallel, cylindrical nanocavities is given by^{10,13,27–29}

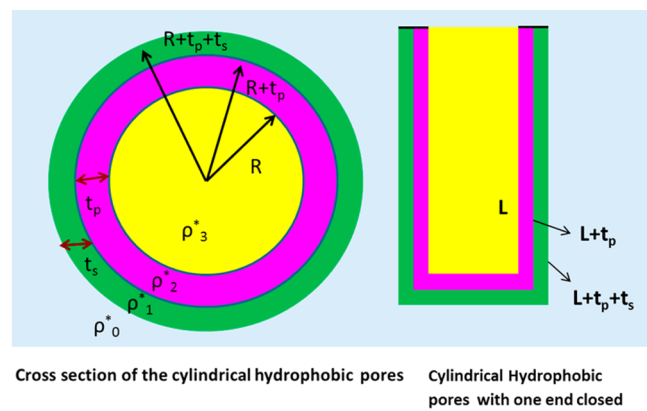
$$I(Q) = KP(Q)S(Q) \quad (1)$$

where K is a Q -independent parameter that is a function of pore volume, $P(Q)$ is the form factor of the core–shell cylindrical pores, and $S(Q)$ is the spherically averaged structure factor that in case of infinitely high resolution is represented by a sum of δ -functions at reciprocal lattice points corresponding to positions of the Bragg diffraction peaks.¹² The changes in the intensity of the Bragg diffraction peaks can be attributed to changes of the form factor as a result of partial filling of the cavities.¹⁰

Geometric model used for calculation of the scattering amplitude and form factor of the core–shell cylindrical cavities is shown in Figure 6. For cylindrical pores with a SiO_2 shell (sample 1) and same pores having an additional shell of the fluoropolymer ($C_{10}H_4Cl_3F_{17}Si$) (sample 2), the scattering amplitude $F(Q)$ is described by equation similar to $F(Q)$ of spherical shells^{13,28,30}

$$\begin{aligned} F(Q) = & (\rho_3^* - \rho_2^*)\pi R^2 L f(Q, R, L) + (\rho_2^* - \rho_1^*)\pi(R + t_p)^2 \\ & \times (L + t_p)f(Q, R + t_p, L + t_p) + (\rho_1^* - \rho_0^*)\pi(R + t_p + t_s)^2 \\ & \times (L + t_p + t_s)f(Q, R + t_p + t_s, L + t_p + t_s) \end{aligned} \quad (2)$$

In eq 2, $\rho_0^* = 2.08 \times 10^{10} \text{ cm}^{-2}$ is the SLD of silicon, $\rho_1^* = 3.47 \times 10^{10} \text{ cm}^{-2}$ is SLD of SiO_2 , $\rho_2^* = 3.18 \times 10^{10} \text{ cm}^{-2}$ is SLD of the fluoropolymer, and ρ_3^* is SLD of the internal cylinder volume filled with air ($\rho_3^* = 0$), D_2O ($\rho_3^* = 6.39 \times 10^{10} \text{ cm}^{-2}$), or contrast matching solution ($\rho_3^* = \rho_0^* = 2.08 \times 10^{10} \text{ cm}^{-2}$) (Table 1). R and L are the radius and length of the internal volume of the cylinder, respectively. t_p and t_s are the thickness of the polymer and silica shell, respectively. For



Cross section of the cylindrical hydrophobic pores Cylindrical Hydrophobic pores with one end closed

Figure 6. Geometric model of the hydrophobically modified cylindrical pores used for calculation of the scattering amplitude and form factor of the hydrophobically modified cavities. Blue: Si matrix; green: SiO_2 layer; magenta: fluoropolymer layer.

sample 1, it is assumed that $\rho_3^* = 0$, $t_p = 0$, $t_s = 2 \text{ nm}$, and the internal length $L = 100 \text{ nm}$. Correspondingly, for sample 2 $t_p = 5 \text{ nm}$ and $L = 100 - 5 = 95 \text{ nm}$. The function $f(Q, R, L)$ is defined as

$$f(Q, R, L) = 2J_0\left(\frac{QL \cos \alpha}{2}\right) \frac{J_1(QR \sin \alpha)}{QR \sin \alpha} \quad (3)$$

where J_0 and J_1 are the first type Bessel function of zero and first order, respectively, and α is the angle between the cylinder axes and the normal to the incident beam.

Form factor of randomly oriented cylinders is given by

$$P(Q) = \int_0^{\pi/2} F^2(Q, \alpha) \sin \alpha \, d\alpha \quad (4)$$

In the case of cylinders oriented parallel to the beam (wafer placed perpendicular to the beam), $\alpha = \pi/2$ and eq 3 reduces to

$$f(Q, R) = 2 \frac{J_1(QR)}{QR} \quad (5)$$

Hence, eq 2 can be rewritten as

$$\begin{aligned} F(Q) = & (\rho_3^* - \rho_2^*)\pi R^2 L f(Q, R, L) + (\rho_2^* - \rho_1^*)\pi(R + t_p)^2 \\ & \times (L + t_p)f(Q, R + t_p) + (\rho_1^* - \rho_0^*)\pi(R + t_p + t_s)^2 \\ & \times (L + t_p + t_s)f(Q, R + t_p + t_s) \end{aligned} \quad (6)$$

and the form factor of such aligned array of cylinders is

$$P(Q) = |F^2(Q)| \quad (7)$$

The main Bragg peak $I(Q_{\text{Bragg}} = 0.0037 \text{ \AA}^{-1})$ is due to contrast between the scattering length density of the solid matrix ρ_s^* (Si with one (SiO_2) or two ($SiO_2 +$ fluoropolymer) shells and the medium filling the cavities ρ_3^* (air, D_2O , or CMS). If the medium fills the cavity to a uniform depth, the intensity can be well approximated as $I \sim (\rho_0^* - \rho_3^*)^2$. For cavities filled with D_2O the peak intensity is expected to increase due to much higher contrast between Si and D_2O compared to that between Si and air (see Table 1). At the same time, for cavities filled with CMS the peak intensity should decrease due to decreasing contrast between the CMS and Si matrix. In the latter case, the volume fraction of cavities that is actually filled with CMS (ϕ_{CMS}) may be approximated by

$$\phi_{\text{CMS}} = \frac{1 - \sqrt{(\text{measured peak ratio})}}{1 - \sqrt{(\text{peak ratio for completely filled cavities})}} \quad (8)$$

A similar formula was used in refs 15 and 16 for calculation of the filling degree of Si cavities filled with H_2O measured using X-ray

scattering. In the two-phase approximation (Si pores filled with H₂O) eq 8 reduces to

$$\phi_{\text{CMS}} = \frac{\rho_{\text{Si}}^*}{\rho_{\text{H}_2\text{O}}^*} [1 - \sqrt{(\text{measured peak ratio})}] \quad (9)$$

For D₂O-filled cylindrical cavities with composite matrix (additional shell of SiO₂ or two shells of SiO₂ + fluoropolymer) the filling degree is evaluated by calculating core–shell cylinder form factor (for the known sizes of the shells and corresponding SLDs) and comparing the ratios of the measured and calculated for the case of complete filling intensities at $I(Q_{\text{Bragg}} = 0.0037 \text{ \AA}^{-1})$

$$\phi_{\text{D}_2\text{O}} = \frac{\sqrt{(\text{measured peak ratio})} - 1}{1 - \sqrt{\text{peak ratio for completely filled cavities}} - 1} \quad (10)$$

Equations 8 and 10 were used in this study to calculate the filling degree of cavities with CMS and D₂O, respectively.

RESULTS AND DISCUSSION

At the main Bragg peak $I(Q_{\text{Bragg}} = 0.0037 \text{ \AA}^{-1})$ for cavities completely filled with D₂O the intensity is expected to increase by a factor of 4.83 and 6.68 for sample 1 and sample 2, respectively, compared to air. Such an increase is significantly higher than if one ignores the SiO₂ and fluoropolymer layers, in which case $\rho_3^* = \rho_2^*$, $\rho_0^* = \rho_1^*$, and $I(Q_{\text{Bragg}})_{\text{D}_2\text{O}}/I(Q_{\text{Bragg}})_{\text{DRY}} = 4.29$. Similarly, when the cavities are completely filled with the CMS, $I(Q_{\text{Bragg}})_{\text{CMS}}/I(Q_{\text{Bragg}})_{\text{DRY}} = 1/356$ for sample 2 is ~1.7 times lower than that for sample 1 ($I(Q_{\text{Bragg}})_{\text{CMS}}/I(Q_{\text{Bragg}})_{\text{DRY}} = 1/595$) due to the presence of the additional fluoropolymer layer. This underlines importance of taking into account the scattering length densities and geometrical features of both SiO₂ and polymer shells when calculating the cavity filling degree.

As is seen in Table 2, the measured increase in scattering from cavities in contact with D₂O is actually much smaller than the predicted for completely saturated cavities due to partial filling. The volume fraction of cavities that is actually filled with D₂O ($\phi_{\text{D}_2\text{O}}$) may be approximated by eq 10,^{15,16} in which (peak ratio for completely filled cavities) is 4.83 or 6.68 for studied samples. Using values of the measured and calculated peak ratios, we calculate the cavity filling degree $\phi_{\text{D}_2\text{O}}$ for samples immersed in D₂O that is shown in Table 2. As is seen, the filling degree of cavities in sample 1 ($\phi_{\text{D}_2\text{O}} = 0.31$ and 0.36) measured in both experiments agree with each other. These numbers imply that about 1/3 of the cavity volume is filled with D₂O. Filling degrees of cavities with hydrophobic walls ($\phi_{\text{D}_2\text{O}} = 0.13$, experiment 1 and $\phi_{\text{D}_2\text{O}} = 0.14$, experiment 2) also agree with each other; however, these numbers are about factor of 3 lower than $\phi_{\text{D}_2\text{O}}$ of less hydrophobic cavities. Thus, in this sample 86–87% of the cavity volume remains filled with vapor after immersing in the CMS. Based on the known average filling degree of cavities in sample 2 with D₂O ($\bar{\phi}_{\text{D}_2\text{O}} \sim 0.135$) and assuming that it remains the same for the contrast matching solution, we calculate the reduction factor of the peak amplitude $1.35/0.056 \approx 24$, which gives the filling degree of cavities in sample 2 $\phi_{\text{CMS}} = 0.19$. This number, although subject to much larger errors due to weak scattering signal from cavities in contact with CMS, agrees reasonably well with the D₂O-based measurements $\phi_{\text{CMS}} = 0.13–0.14$. The above-mentioned invariance of the scattering with time during the experiment

demonstrates that formed air nanobubbles remain stable during at least several hours.

The presented data demonstrate the high degree of sensitivity of SANS measurements for detecting and characterizing monolayers of nano- and mesoscale bubbles formed on the surface of different materials with the volume fraction as low as $\sim 10^{-6}$ (volume of bubbles per cubic centimeter). We found that the filling fraction of nanoscale cavities (or size of trapped nanobubbles) depends strongly on the surface wettability. The volume of trapped nanobubbles may occupy as much as $\sim 87\%$ of the cavity volume for strongly hydrophobic surfaces and $\sim 2/3$ of the cavity volume in case of moderately hydrophobic surfaces. Filling fraction of the studied 100 nm cavities covered with fluoropolymer (sample 2) ($\phi_{\text{D}_2\text{O}} = 0.13–0.14$) is similar to that of the 100 nm deep cylindrical pores with much smaller diameter ~ 28 nm modified with an hydrophobic octadecyltrichlorosilane monolayer ($\phi_{\text{D}_2\text{O}} = 0.12$ ¹⁵). This suggests that the surface wettability has a greater influence on the formation of nanobubbles in cavities of these length scales than the cavity geometry. At the same time, our findings demonstrate that relatively moderate hydrophobicity of nanostructured surfaces characterized by contact angles below 90° is sufficient for high density of interfacial nanobubbles to be formed. The detected nanobubbles are stable with time for at least several hours, which confirms the conclusion that dewetted and partially dewetted hydrophobic pores may be thermodynamically stable in contact with water under ambient pressure and temperature.¹⁵ Furthermore, experimental approaches demonstrated in the present study open up an excellent opportunity to conduct systematic quantitative investigations of the variations in the filling fraction as a function of the cavity shape at different pressures and temperatures.

AUTHOR INFORMATION

Corresponding Author

*E-mail melnichenkoy@ornl.gov (Y.B.M.).

Notes

The authors declare no competing financial interest.

ACKNOWLEDGMENTS

The research at Oak Ridge National Laboratory's High Flux Isotope Reactor was sponsored by the Laboratory Directed Research and Development Program and the Scientific User Facilities Division, Office of Basic Energy Sciences, U.S. Department of Energy. Preparation of nanostructured surface was conducted at the Center for Nanophase Materials Sciences, which is sponsored at Oak Ridge National Laboratory by the Scientific User Facilities Division, Office of Basic Energy Sciences, U.S. Department of Energy. This research was supported in part by the ORNL Postdoctoral Research Associates Program, administered jointly by the ORNL and the Oak Ridge Institute for Science and Education. This research project has been supported in part by the European Commission under the seventh Framework Programme through the 'Research Infrastructures' action of the 'Capacities' Programme, NMI3-II Grant number 283883.

REFERENCES

- (1) Theofanous, T. G.; Tu, J. P.; Dinh, A. T.; Dinh, T. N. The boiling crisis phenomenon - Part I: nucleation and nucleate boiling heat transfer. *Exp. Therm. Fluid Sci.* 2002, 26 (6-7), 775–792.

- (2) Bang, I. C.; Jeong, J. H. Nanotechnology for advanced nuclear thermal-hydraulics and safety: boiling and condensation. *Nucl. Eng. Technol.* **2011**, *43* (3), 217–242.
- (3) Dizon, M. B.; Yang, J.; Cheung, F. B.; Rempe, J. L.; Suh, K. Y.; Kim, S. B. Effects of surface coating on the critical heat flux for pool boiling from a downward facing surface. *J. Enhanced Heat Transfer* **2004**, *11* (2), 133–150.
- (4) Yang, S. R.; Kim, R. H. A mathematical-model of the pool boiling nucleation site density in terms of the surface characteristics. *Int. J. Heat Mass Transfer* **1988**, *31* (6), 1127–1135.
- (5) Wang, C. H.; Dhir, V. K. Effect of surface wettability on active nucleation site density during pool boiling of water on a vertical surface. *J. Heat Transfer* **1993**, *115* (3), 659–669.
- (6) Gerardi, C.; Buongiorno, J.; Hu, L. W.; McKrell, T. Experimental observation of the dynamic micro- and macro-layer during pool boiling. Proceedings of 2008 ASME Summer Heat Transfer Conference, HT2008, August 10–14, 2008, Jacksonville, FL, HT2008-56010.
- (7) White, E. R.; Mecklenburg, M.; Singer, S. B.; Aloni, S.; Regan, B. C. Imaging nanobubbles in water with scanning transmission electron microscopy. *Appl. Phys. Express* **2011**, *4* (5).
- (8) Brown, R. J. C.; Evans, M. J. B.; Tun, Z. Neutron scattering study of adsorption in porous MCM-41 silica. *Can. J. Phys.* **2010**, *88* (10), 707–713.
- (9) Broseta, D.; Barre, L.; Vizika, O.; Shahidzadeh, N.; Guilbaud, J. P.; Lyonnard, S. Capillary condensation in a fractal porous medium. *Phys. Rev. Lett.* **2001**, *86* (23), 5313–5316.
- (10) Findenegg, G. H.; Jahnert, S.; Muter, D.; Prass, J.; Paris, O. Fluid adsorption in ordered mesoporous solids determined by in situ small-angle X-ray scattering. *Phys. Chem. Chem. Phys.* **2010**, *12* (26), 7211–7220.
- (11) Mascotto, S.; Wallacher, D.; Brandt, A.; Hauss, T.; Thommes, M.; Zickler, G. A.; Funari, S. S.; Timmann, A.; Smarsly, B. M. Analysis of microporosity in ordered mesoporous hierarchically structured silica by combining physisorption with in situ small-angle scattering (SAXS and SANS). *Langmuir* **2009**, *25* (21), 12670–12681.
- (12) Pollock, R. A.; Walsh, B. R.; Fry, J.; Ghompson, I. T.; Melnichenko, Y. B.; Kaiser, H.; Pynn, R.; DeSisto, W. J.; Wheeler, M. C.; Frederick, B. G. Size and spatial distribution of micropores in SBA-15 using CM-SANS. *Chem. Mater.* **2011**, *23* (17), 3828–3840.
- (13) Zickler, G. A.; Jahnert, S.; Wagermaier, W.; Funari, S. S.; Findenegg, G. H.; Paris, O. Physisorbed films in periodic mesoporous silica studied by in situ synchrotron small-angle diffraction. *Phys. Rev. B* **2006**, *73* (18).
- (14) He, L. L.; Chathoth, S. M.; Melnichenko, Y. B.; Presser, V.; McDonough, J.; Gogotsi, Y. Small-angle neutron scattering characterization of the structure of nanoporous carbons for energy-related applications. *Microporous Mesoporous Mater.* **2012**, *149* (1), 46–54.
- (15) Checco, A.; Hofmann, T.; DiMasi, E.; Black, C. T.; Ocko, B. M. Morphology of air nanobubbles trapped at hydrophobic nanopatterned surfaces. *Nano Lett.* **2010**, *10* (4), 1354–1358.
- (16) Checco, A.; Ocko, B. M.; Rahman, A.; Black, C. T.; Tsinkevych, M.; Giacomello, A.; Dietrich, S. Collapse and reversibility of the superhydrophobic state on nanotextured surfaces. *Phys. Rev. Lett.* **2014**, *112* (21), 216101.
- (17) Zhang, H.; Lamb, R. N.; Cookson, D. J. Nanowetting of rough superhydrophobic surfaces. *Appl. Phys. Lett.* **2007**, *91* (25).
- (18) Smith, G. S.; Jung, S. Y.; Browning, J. F.; Keum, J. K.; Lavrik, N. V.; Alemsegued, M. G.; Collier, C. P. Bilayer self-assembly on a hydrophilic, deterministically nanopatterned surface. *Nano Res.* **2013**, *6* (11), 784–794.
- (19) Bhandari, D.; Kravchenko, II; Lavrik, N. V.; Sepaniak, M. J. Nanotransfer printing using plasma etched silicon stamps and mediated by in situ deposited fluoropolymer. *J. Am. Chem. Soc.* **2011**, *133* (20), 7722–7724.
- (20) Agrawal, A.; Park, J.; Ryu, D. Y.; Hammond, P. T.; Russell, T. P.; McKinley, G. H. Controlling the location and spatial extent of nanobubbles using hydrophobically nanopatterned surfaces. *Nano Lett.* **2005**, *5* (9), 1751–1756.
- (21) Smirnov, S. N.; Vlassiouk, I. V.; Lavrik, N. V. Voltage-gated hydrophobic nanopores. *ACS Nano* **2011**, *5* (9), 7453–7461.
- (22) Feng, B.; Weaver, K.; Peterson, G. P. Enhancement of critical heat flux in pool boiling using atomic layer deposition of alumina. *Appl. Phys. Lett.* **2012**, *100* (5).
- (23) Lu, Y. W.; Kandlikar, S. G. Nanoscale surface modification techniques for pool boiling enhancement. A critical review and future directions. *Heat Transfer Eng.* **2011**, *32* (10), 827–842.
- (24) Ahn, H. S.; Kim, M. H. A review on critical heat flux enhancement with nanofluids and surface modification. *J. Heat Transfer* **2012**, *134* (2).
- (25) Yao, Z.; Lu, Y. W.; Kandlikar, S. G. Effects of nanowire height on pool boiling performance of water on silicon chips. *Int. J. Therm. Sci.* **2011**, *50* (11), 2084–2090.
- (26) Betz, A. R.; Xu, J.; Qiu, H. H.; Attinger, D. Do surfaces with mixed hydrophilic and hydrophobic areas enhance pool boiling? *Appl. Phys. Lett.* **2010**, *97* (14).
- (27) Marchal, D.; Deme, B. Small-angle neutron scattering by porous alumina membranes made of aligned cylindrical channels. *J. Appl. Crystallogr.* **2003**, *36*, 713–717.
- (28) Pedersen, J. S. Analysis of small-angle scattering data from colloids and polymer solutions: modeling and least-squares fitting. *Adv. Colloid Interface Sci.* **1997**, *70*, 171–210.
- (29) Smarsly, B.; Goltner, C.; Antonietti, M.; Ruland, W.; Hoinkis, E. SANS investigation of nitrogen sorption in porous silica. *J. Phys. Chem. B* **2001**, *105* (4), 831–840.
- (30) Engel, M.; Stuhn, B.; Schneider, J. J.; Cornelius, T.; Naumann, M. Small-angle X-ray scattering (SAXS) off parallel, cylindrical, well-defined nanopores: from random pore distribution to highly ordered samples. *Appl. Phys. A: Mater. Sci. Process.* **2009**, *97* (1), 99–108.